Propagation of positive discharges in an air bubble having an embedded water droplet

Wenjun Ning[1,2]**, Janis Lai**[3]**, Juliusz Kruszelnicki**[3]**, John E Foster**[3]**, Dong Dai**[4] **and Mark J Kushner**[2,*]

[1] College of Electrical Engineering, Sichuan University, Chengdu, 610065, People's Republic of China
[2] Department of Electrical Engineering and Computer Science, University of Michigan, 1301 Beal Avenue, Ann Arbor, MI 48109-2122, United States of America
[3] Department of Nuclear Engineering and Radiological Sciences, University of Michigan, 2355 Bonisteel Boulevard, Ann Arbor, MI 48109-2104, United States of America
[4] School of Electrical Power, South China University of Technology, Guangzhou, 510641, People's Republic of China

E-mail: ningwj@scu.edu.cn, janislai@umich.edu, jkrusze@umich.edu, jefoster@umich.edu, ddai@scut.edu.cn and mjkush@umich.edu

Abstract

Low temperature plasmas generated inside gas bubbles immersed in water is an effective method of rapidly transferring plasma generated reactive species to the water for applications in biomedicine, agriculture and environment. Reactive species are generally produced in the gas phase plasma and then solvate into the liquid. The large surface-to-volume ratio (SVR) of the bubble accelerates this process. In generating bubbles in water, aerosols and droplets are also contained within the bubble. These droplets also have a large SVR and so can be rapidly plasma activated. However, the presence of the droplets can also impact the propagation of the plasma in the bubble. In this paper, results are discussed from computational and experimental investigations of the formation and evolution of discharges in an air bubble immersed in water with an embedded water droplet. The computations were performed with a two-dimensional plasma hydrodynamics model. Experiments were performed with a quasi-2D bubble apparatus. In bubbles having a droplet, a plasma filament typically bridges from the powered electrode to the droplet, and then from the droplet to the bubble surface. A surface-hugging streamer also occurs on the inner bubble surface and on the surface of the droplet. Both surface streamers result in part from surface charge accumulation and can dominate the formation of reactive species that transport into the droplet. Increasing droplet conductivity suppresses propagation of the surface discharge and leads to a lower density of aqueous reactive species. Increasing conductivity of the surrounding water does not change the overall structure of the discharge but does slightly elevate the discharge intensity. The size and shape of the embedded droplet can significantly affect the formation and propagation of the streamer.

Keywords: plasma-water interactions, modeling, multiphase

(Some figures may appear in colour only in the online journal)

1. Introduction

Atmospheric pressure plasma-liquid interactions are rich sources of reactive oxygen and nitrogen species (RONS) in the liquid that play important roles in biomedicine, environmental remediation, agriculture and food safety [1–6]. In these applications, there are generally two processes that need to be optimized—ignition of the discharge and production of primary active species, which occurs mostly in the gas phase; and the transport of these reactive species into liquid phase where

---

* Author to whom correspondence should be addressed.

they may subsequently produce secondary species. The ability to produce RONS at near ambient temperatures has enabled atmospheric pressure plasmas to activate heat sensitive liquids and surfaces, such as living tissue in plasma medical therapy [7–10].

The gas–liquid reactors intended to generate low temperature plasmas for activation of the liquid can be classified into at least three configurations. In the first, plasma is produced and sustained in the gas region above and independent of the liquid surface [11–16]. The plasma source can be an atmospheric pressure plasma jet, where the liquid acts as a downstream substrate. In the second, the liquid acts as an electrode. For example, a pin-plate discharge or dielectric barrier discharge (DBD) has one electrode in the gas phase and a second inside the liquid [17, 18]. In both configurations, reactive species transport from the plasma to the gas–liquid interface and solvate into the liquid, although photolysis by (V)UV radiation or direct charge exchange of gas phase ions with the liquid can also produce in-liquid reactive species. These processes are subject to transport limits in the reactive species convecting or diffusing from their site of formation to the liquid interface. This is particularly problematic for short-lived species [19, 20].

A third method is to sustain discharges in gas bubbles that are immersed in the liquid. The gas bubble can either be self-generated by an enthalpy change produced by the discharge or be purposely injected into the liquid. Due to the density of the liquid typically being 1000 times that of a gas at atmospheric pressure, the electric field strength required to electrically breakdown the liquid is orders of magnitude higher than in the gas. The large electric field required to initiate a plasma in a liquid leads to the majority of discharges inside dielectric liquids occurring in (or being initiated in) bubbles. Even in degassed water, there likely exists bubbles having sizes of 100's nm [21]. When micro bubbles are injected into a liquid, the formative lag time to initiate a discharge is significantly decreased [22–24].

With these observations, research has focused on the properties of plasmas in bubbles in liquids. These studies have varied parameters such as the gas composition inside the bubble [25–28], permittivity or conductivity of the liquid [29–35], geometry of the bubble [36–39], electrode arrangement [27, 38, 40] and power sources [41]. For example, Babaeva and Kushner [29] proposed that two discharge modes could occur in an air bubble submerged in liquid depending on the relative permittivity ε_r of the liquid. For low ε_r a volume streamer usually occurs. For large ε_r a surface-hugging streamer occurs. The applied voltage amplitude, bubble size and liquid conductivity also affect the discharge pattern inside the bubble. From the point view of activating the surrounding liquid, the surface-hugging streamer may be preferred for the rapid solvation of gas-phase reactive species into liquid. Tachibana *et al* [25] proposed that the gas composition was another important factor in determining the discharge pattern. They experimentally observed volume discharges (diffusive or filamentary) for He or Ar filled bubbles, while surface discharges were observed for N_2 filled bubbles. The findings were supported by Tian's simulation results [26]. Tu *et al* [38], Sommers and Foster

[42], and Hamdan and Cha [27] emphasized the importance of the relative position between bubbles and electrodes in the formation of surface or volumetric discharges.

To address the transport limits of reactive species to liquid interfaces, especially for large scale liquid treatment, a promising method is to activate small liquid droplets immersed in plasma. The intrinsically large surface-to-volume ratio (SVR) of droplets and short transport distance from site of creation in the plasma to the droplet surface improve activation efficiency. Experiments have demonstrated efficient plasma activation of water droplets and mist, and effective inactivation of biofilms or bacteria using these activated droplets and mist [43, 44]. Having said that, a mist of small liquid droplets could affect the composition of the gas through evaporation and produce electric field distortion, and so affect the physical-chemical properties of the plasma. Wandell and Locke [45] showed particularly high concentrations of H_2O_{2aq} (the suffix aq means aqueous state) in plasma treated water droplets. Kruszelnicki *et al* [46] conducted computational investigations on the dominant pathways of producing reactive species and the spatial-temporal processes of activating water droplets by an air DBD. The transport limits of gas-phase reactive species into their aqueous counterparts were found to depend on their Henry's law constant, droplet size and plasma uniformity.

In plasma activation of water using the plasma-in-bubble technique, it is often the case that large bubbles also contain water aerosols and droplets. These immersed droplets may form in a turbulent or highly mixed environment, or during the bubble formation process. In some ways this is advantageous. The droplet has a large SVR and is immersed in the plasma produced in the bubble, which accelerates the activation of the droplet. At the same time, the immersed droplet can significantly affect the propagation of the discharge inside the bubble.

In this paper, we discuss results from computational and experimental investigations of atmospheric pressure discharges inside a two-dimensional (2D) air bubble surrounded by water and containing a water droplet. Our discussion focuses on the effects of the water droplet on discharge ignition and propagation. The computed discharge patterns systematically agree with experimental images captured using an intensified charge-coupled device (ICCD). The water droplet inside the air bubble tends to trigger filamentary discharges that bridge the spaces between the anode, droplet surface and bubble surface, in addition to a surface-hugging streamer on the bubble surface. The plasma filament between the droplet surface and bubble surface is triggered by the enhanced electric field resulting from droplet polarization and seed electrons provided by photoionization. A surface streamer can develop on the droplet surface due to charge accumulation, which can dominate delivery of reactive species to the droplet. As such, lower conductivity of the droplet can enhance the solvation of reactive species. On the other hand, increasing the conductivity of the surrounding water can increase the discharge intensity in the bubble to produce more reactive, shorter-lived species such as OH_{aq}. The influence of bubble shape and droplet size are also discussed from the perspective of discharge dynamics.

The model, geometry and experiment setup are described in section 2. The evolution of plasma filaments and surface streamers for the base case, as well as the consequences of conductivity, bubble deformation and droplet size are discussed in section 3. Concluding Remarks are made in section 4.

2. Description of the model and experiment

2.1. Model

The numerical investigation was performed with *nonPDP-SIM*, a two-dimensional multi-fluid hydrodynamics simulation which has been described in detail in references [46, 47]. Briefly, the continuity equations for each species, electron energy conservation equation, radiation transport in the form of a Green's function formulation and Poisson's equation are implicitly integrated in a time-marching fashion. The first three sets of equations are solved in the plasma region (the air bubble and the water droplet), while Poisson's equation is integrated over the entire computational domain. Boltzmann's equation is solved for the electron energy distribution to provide electron transport and rate coefficients as a function of electron mean energy. These values were updated every 0.1 ns during the simulation to account for the transient evolution of discharge dynamics and composition of the gas.

The plasma region consisted of the gas-phase humid air in the bubble and the liquid-phase water (droplet), which are distinguished by specifying separate zones in the numerical mesh. Computationally and algorithmically, the two zones are treated identically, while different reaction mechanisms, permittivity and transport coefficients are separately employed for the gaseous and liquid zones. The water droplet has a large permittivity ($\approx 80\varepsilon_0$), which is included in the model by calculating the number density weighted polarizability for all species in the water, a value that would typically be updated every ns. If there was a significant change in density or mole fraction of a species in the water, the permittivity would reflect this change. However, since the mole fraction of species produced in the water is small, from a practical perspective the permittivity does not significantly deviate from $80\varepsilon_0$. For the conditions of this study, there is essentially no change in permittivity in either zone. Transport coefficients for neutral and charged species between numerical nodes are determined by the local densities at the adjacent mesh nodes. The exception is for the gas–liquid boundary layer, where limits on transport given by Henry's law equilibrium were taken into consideration.

The water surrounding the bubble was modeled as a non-reacting lossy dielectric with a constant permittivity of $80\varepsilon_0$ and specified conductivity ranging from zero to 1.3×10^{-2} S cm^{-1}. The equations solved in the water surrounding the bubble are Poisson's equation for the electric potential and a continuity equation for charge density, ρ_w,

$$\frac{\partial \rho_w}{\partial t} = -\nabla \cdot \vec{j} - \left[\sum_k \nabla \cdot q_k \vec{\phi}_k s_k (1 + \gamma_k) \right]_b, \quad \vec{j} = \sigma \vec{E}. \quad (1)$$

Here, $\vec{j}$ is the current density, σ is the water conductivity and $\vec{E}$ is the electric field. The term in brackets is only included at the boundary of the water, and includes contributions from the fluxes of species k having charge q_k, flux $\vec{\phi}_k$, neutralization (or collection) probability on the surface of s_k and secondary electron emission coefficient of γ_k, This technique accounts for polarization of the surrounding water and charge redistribution.

Henry's law describes the equilibrium between the density of a gas dissolved in a liquid and the partial pressure of the gas in the vapor phase for a given temperature [48]. The flux of a gas-phase species into a liquid is therefore limited by the approach to equilibrium at the gas–liquid interface. If the gas–liquid interface is at equilibrium (that is, saturated) with the gas phase species, net transport of that species into the interface will cease. This process is represented in the model as follows. The gas-phase species at the numerical mesh node adjacent to the liquid interface has density n_g and diffusion coefficient D_g. Its liquid-phase counterpart has density n_l at the liquid surface with a Henry's law equilibrium constant h [46, 49]. The gas-phase flux $\Gamma_{g \to l}$ entering the liquid is:

$$\Gamma_{g \to l} = \begin{cases} D_g \dfrac{(n_g h - n_l)}{n_g h} \dfrac{(n_g - n_l)}{\Delta x}, & (n_g h - n_l \geqslant 0) \\ 0, & (n_g h - n_l < 0) \end{cases}, \quad (2)$$

where Δx is the spacing between the gas and liquid mesh nodes. $\Gamma_{g \to l}$ equaling zero means the solvated species is saturated at the liquid surface. The high density of the solvated species at the surface of the liquid results in diffusion into the liquid, thereby reducing the density at the surface. The reduction of density at the surface then enables additional gas phase flux to enter the liquid. The liquid-phase species transports into the gas phase with a flux of $\Gamma_{l \to g}$:

$$\Gamma_{l \to g} = \begin{cases} D_l \dfrac{(n_l - n_g h)}{n_l} \dfrac{(n_l - n_g)}{\Delta x}, & (n_l - n_g h \geqslant 0) \\ 0, & (n_l - n_g h < 0) \end{cases}, \quad (3)$$

where D_l is the liquid-phase diffusion coefficient.

Gas-phase charged species (electron and ions) are allowed to directly enter the liquid with the gas-phase rate of diffusion (and drift in electric field). However, the liquid-phase ions are not allowed to exit from the liquid, given their low transport coefficients, and large solvation and charge exchange rate.

For numerical accounting purposes, once the gas-phase species enters the liquid, it is transformed into an aqueous species (here denoted by a subscript aq). The rates of solvation are usually rapid due to naturally occurring reactions with H_2O_{aq}. In the absence of known rates from the literature, an estimated rate of solvation is used to prevent gas phase species from having a significant density in the liquid phase. Gas phase electrons entering into the water quickly interact with polar water molecules to form a solvated electron, H_2O-e_{aq} (denoted as e_{aq} in the text for simplicity), which then tends toward equilibrium with water to form H_{aq} and OH_{aq}^-. Most of the gas phase positive ions entering the water undergo charge exchange with H_2O_{aq} to form $H_2O_{aq}^+$, rapidly followed by charge exchange with H_2O_{aq} to form $H_3O_{aq}^+$ and OH_{aq}. The latter is an important process contributing to the production of the hydroxyl radical. VUV photons are emitted by highly
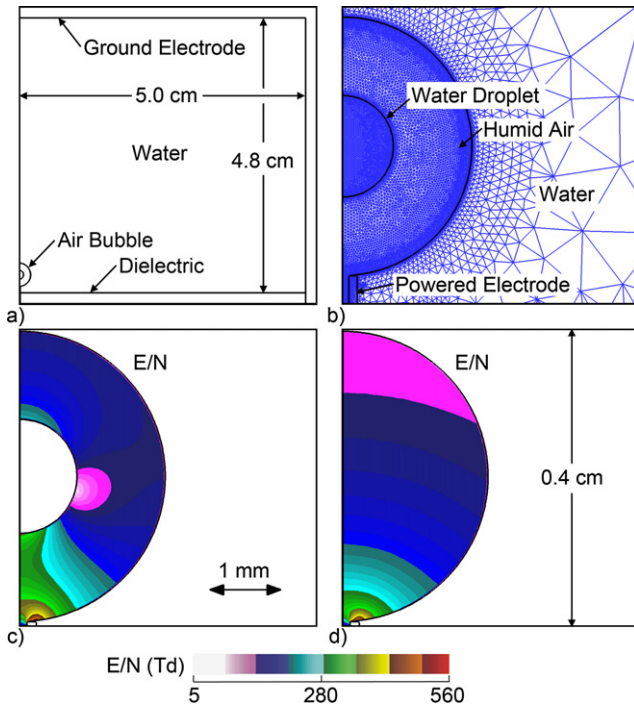
Figure 1. Schematic of the model. (a) Entire computational domain. (b) Enlarged view of the plasma region (air bubble and water droplet) and the unstructured mesh. (c) Spatial distribution of reduced electric field *E/N* without plasma (applied voltage 20 kV). (d) *E/N* without water droplet.

Figure 2. Schematic of experimental setup.

excited electronic states of N_2 in the gas phase, denoted as N_2^{**} (a lumped state including transitions higher than $N_2(A^3\Sigma)$, such as $N_2(C^3\Pi)$ and $N_2(E^3\Sigma)$) which photoionize O_2 and H_2O in the gas phase. VUV photons entering the water ionize and dissociate H_2O_{aq} [26]. The plasma chemistry reaction mechanism includes 58 gas-phase species and 36 liquid-phase species, which contribute to 1494 reactions (156 reactions involved with liquid-phase species). The reaction mechanisms and pathways are described in detail in references [46–48].

Photoionization is addressed using a Green's function approach, which is described in detail in reference [50]. Briefly, the photoionization source for species m at location $\vec{r}_i$ due to the emission of photons at location $\vec{r}_j$ by species k is

$$S_m(\vec{r}_i) = \sigma_{km}^I N_m(\vec{r}_i) A_k \int N_k(\vec{r}_j') G_k(\vec{r}_j', \vec{r}_i) \, d^3\vec{r}_j' \quad (4)$$

$$G_k(\vec{r}_j', \vec{r}_i) = \frac{1}{4\pi|\vec{r}_j' - \vec{r}_i|^2} \exp\left[-\int_{\vec{r}_j'}^{\vec{r}_{in}'} \sum_l \sigma_{lk} N_l(\vec{r}_n') \, d\vec{r}_n'\right], \quad (5)$$

where N_k is the density of the radiating species having the Einstein coefficient A_k, σ_{km}^I is the photoionization cross section for species m by photons emitted by species k, and σ_{lk} is the total absorption cross section for photon k by species l. $G_k(\vec{r}_j', \vec{r}_i)$ is a Green's function for the survival of the photons emitted at the location $\vec{r}_j$ to reach location $\vec{r}_i$. The Green's function accounts for absorption of photons, isotropic expansion of the wave front, view angles and obscurations. A discussion of the advantages and weakness of this approach, and comparison to
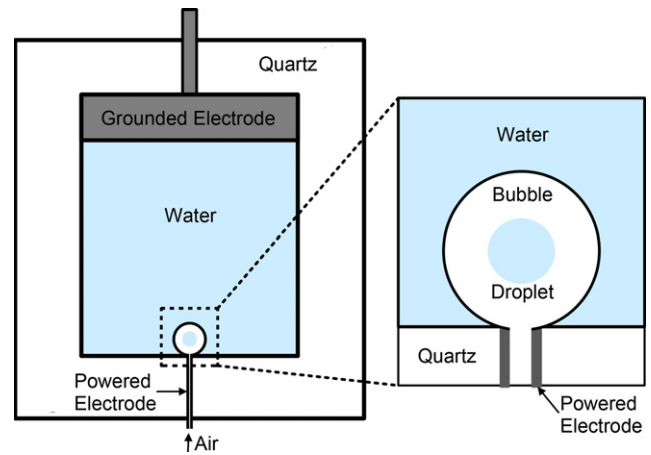
other methods, such as statistical techniques are in reference [50].

The 2D-Cartesian geometry used in the model is shown in figure 1 and is based on the experiments of Lai and Foster [51]. The geometry is symmetric across the left boundary. A gas bubble with diameter of 0.4 cm is surrounded by dielectric water ($\varepsilon_r = 80$). A water droplet with diameter of 0.16 cm in the base case is at the center of the bubble. A hollow powered electrode with inner diameter of 0.02 cm and outer diameter of 0.046 cm connects to the bottom of the gas bubble, while the grounded electrode is 4.28 cm from the bubble boundary. The numerical mesh consisted of 12 217 nodes, with 6449 nodes in the plasma region. In some cases, the dielectric water surrounding the bubble has a conductivity to enable charge transport out of the bubble. As a result, almost 45% of the nodes are expended in the dielectric water. On the surfaces of the bubble and droplet, the mesh size is refined to about 10 μm to resolve the large plasma gradient near the boundaries. A single calculation of 20 ns of discharge dynamics takes up to 2 weeks when the code is running in serial mode on a Linux Server (Intel Xeon(R) E5 3.1 GHz, 256 GB memory). When running in parallel mode, the calculation takes a few days.

The discharge was triggered by a single voltage pulse that rises to 20 kV in 0.1 ns and falls at the end of 10 ns to 0 kV in 1 ns. A neutral plasma cloud with peak electron density of 10^{11} cm^{-3} and radius of 0.01 cm is placed near the powered electrode to provide seed electrons. Tests showed that the density and size of the seed plasma affected the discharge formation time but made only a minor difference to the final results. The gas bubble is filled with atmospheric pressure air (N_2 and O_2) and saturated water vapor (27 Torr at 300 K). The droplet is water with dissolved O_{2aq} of 8 ppm [47] and an initial pH value of 7 (the pH value is determined by the density of $H_3O_{aq}^+$, and OH_{aq}^-, in this case 6×10^9 cm^{-3}). On the surface of the bubble interfacing the dielectric water, charge accumulates consistent with the charged particle fluxes onto the surface and conduction currents through the water. All ion or excited species are quenched to their ground state counterparts on the dielectric water. On the anode surface exposed
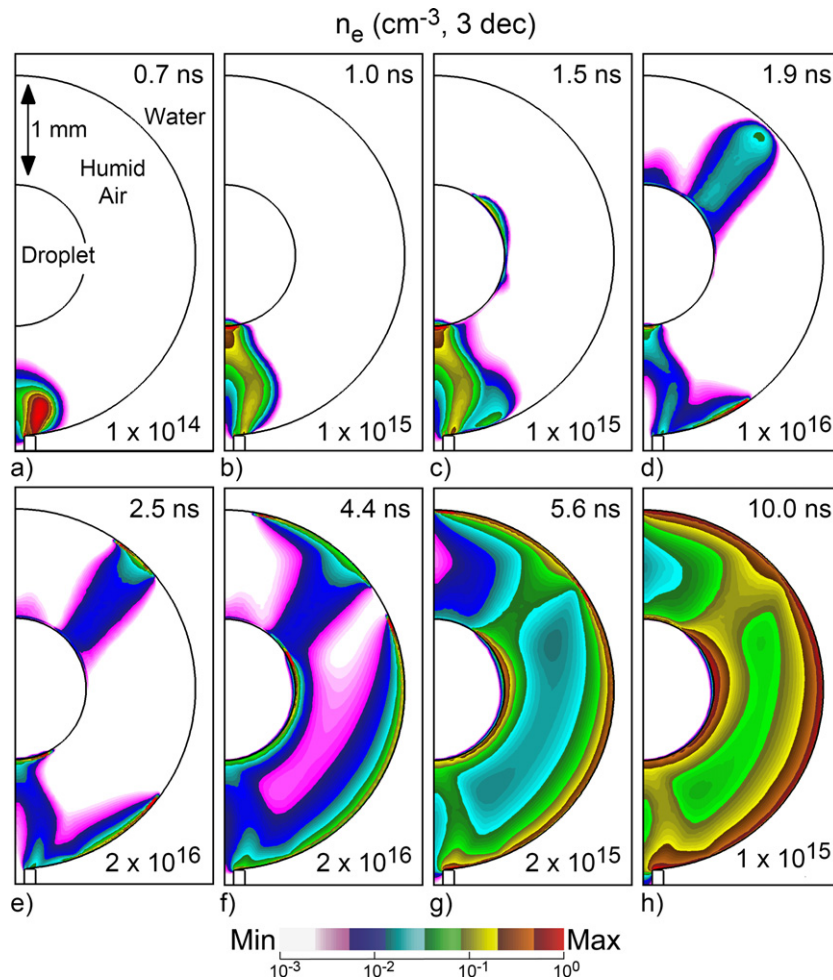
Figure 3. Electron density (n_e, in $\log_{10}$ scale over 3 decades) for the base case at (a) 0.7 ns, (b) 1.0 ns, (c) 1.5 ns, (d) 1.9 ns, (e) 2.5 ns, (f) 4.4 ns, (g) 5.6 ns and (h) 10.0 ns. The maximum value is shown in each frame.

to plasma, secondary electrons are emitted by ion bombardment with a coefficient of 0.15. Considering this investigation focuses on the discharge dynamics over one single voltage pulse of 10 ns, gas heating and convection [52–54], and discharge-induced deformation [55] are not included in the model.

The conductivity of the water droplet, σ_d, was controlled by adding cation–anion pairs akin to salt ions. These cation–anion pairs contribute to the conductivity of the droplet by virtue of their transport properties but do not participate in any reactions in the aqueous chemistry.

2.2. Experiment

ICCD imaging was performed of the discharge dynamics of a bubble in water with an immersed droplet. The quasi-2D apparatus used in this experiment, shown in figure 2, is discussed in reference [51] and is briefly described here. A thin layer of water approximately 0.5 mm thick was trapped between two quartz plates. This confinement was facilitated by a recessed area with dimensions of 30 mm by 30 mm etched into the bottom quartz plate which acted as a liquid reservoir. A channel with diameter of 0.47 mm was also etched in the bottom quartz plate connecting the reservoir with the edge of the quartz plate.

A 10 μl syringe with a 26 gauge blunted needle was threaded into the channel, which served as the gas inlet and the anode. A 2 mm thick stainless-steel plate was embedded on the other end of the reservoir and acted as the cathode. Ambient air was fed into the reservoir and to produce a bubble at the tip of the needle. A gas bubble of approximately 4 mm across was first injected with the syringe. A water droplet approximately 1.6 mm in diameter was then injected into the center of the bubble using the same syringe. This produced the geometry of a pin-to-plane discharge with a suspended dielectric in between the discharge gap.

A nanosecond pulsed power supply (Eagle-Harbor Technology) was used to initiate streamer discharges inside the bubble. Individual pulses with a peak voltage of +20 kV, pulse width of 120 ns and a rise time of approximately 25 ns were applied in this study. Time-resolved images of streamer discharges inside the bubble were taken in a similar fashion as described in reference [51]. Light emission from the plasma was recorded using an Andor iStar 334T ICCD coupled with a Nikon DSLR camera lens. A delay generator (BNC, Model 565) was used to vary the time between triggers for the camera and the power supply, which ranged from 0 to several microseconds. Exposure time used in this study was 5 ns.
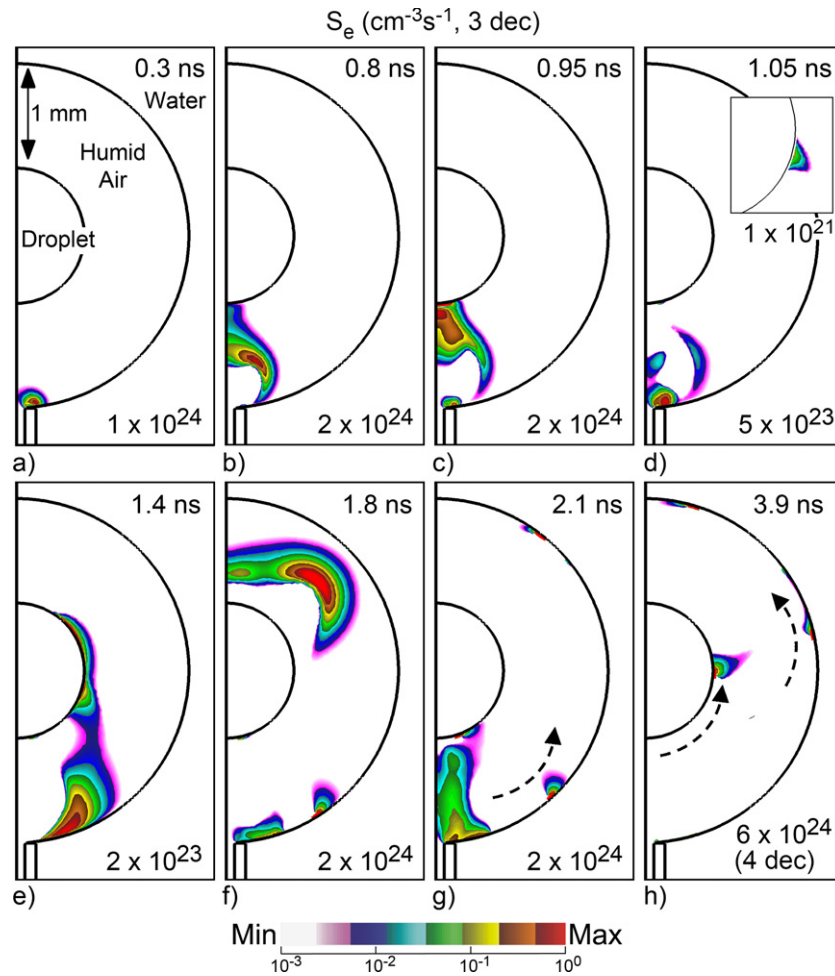
Figure 4. Electron impact ionization source (S_e, in $\log_{10}$ scale over 3 decades unless otherwise noted) for the base case at (a) 0.3 ns, (b) 0.8 ns, (c) 0.95 ns, (d) 1.05 ns, (e) 1.4 ns, (f) 1.8 ns, (g) 2.1 ns and (h) 3.9 ns. The maximum value is shown in each frame. The embedded image in (d) shows a 100-times-intensity enhanced view. The arrows in (h) indicate the direction of propagation of surface discharges.

3. Streamer interactions in the bubble-droplet system

3.1. Base case

For the base case using the geometry shown in figure 1, the water in the droplet is deionized with a pH of 7 and conductivity of 10^{-6} S cm^{-1}, while the water surrounding the bubble is treated as pure dielectric (no conductivity). The applied (Laplacian) electric field, expressed as E/N (electric field/gas (or liquid) number density) peaks in the vicinity of the powered electrode, as shown in figure 1(c). (The units of E/N are Townsend, 1 Td = 10^{-17} V cm^2.) The electric field is enhanced in the region between the droplet and the powered electrode by the natural polarization of the high permittivity of the droplet. For this geometry, the polarization increases the electric field near the vertical poles and decreases the electric field at the equator. The electron density is shown in figure 3 during avalanche and propagation of the discharge following application of the voltage. The corresponding electron impact ionization sources are shown in figure 4.

The discharge initiates at the location of the seed plasma where the electric field is maximum at the edge of the electrode. With electric field enhancement due to the polarization of the droplet, an ionization wave (IW) propagates toward the south pole of the droplet with the ionization front reaching the droplet surface in about 1 ns (figure 3 at 1.0 ns and figure 4 at 0.95 ns). The plasma filament forms a bridge between the powered electrode and the droplet, and stays active while charging the capacitance of the droplet. With the dielectric relaxation time of the droplet being long compared to the propagation time of the filament, the surface of the droplet charges producing a local electron density of 1×10^{15} cm^{-3} with a peak electron-impact ionization rate of 2×10^{24} cm^3 s^{-2}. The filament is a conductive channel which sustains a restrike or reverse IW that propagates from the droplet surface to the powered electrode (figure 4, 1.05 ns). The restrike is a result of an impedance mismatch between the filament channel and the droplet [56, 57]. The charging of the droplet surface also initiates a surface ionization wave (SIW) which propagates upwards toward the equator.

Following the restrike at about 1.5 ns (figure 3 at 1.5 ns and figure 4 at 1.4 ns) the SIW propagates above the equator into a region of enhanced electric field that results from the polarization of the droplet. At this juncture, a second filament propagates from the droplet and to the surface of the bubble at 1.9 ns. A SIW is launched along the surface of the bubble from the electrode while a second SIW propagates along the surface of the droplet [26, 29]. Note that since there is no ballast resistor to reduce voltage across the bubble, the voltage remains at the applied value. When the second IW launched from the top half of the droplet arrives at the bubble surface, a conductive channel forms from the electrode, through the initial filament, along the surface of the droplet and through the second filament to the surface of the bubble. This filament will remain active as long as there is sufficient voltage and the capacitance of the surface of the bubble has not fully charged. Akin to a DBD the surface of the water locally charges at the site of the second filament, which produces a SIW (the foot of the filament in DBD) that propagates in both directions [58, 59]. Due to the charging of both the droplet and of the surface of the bubble, ionization ends first in the filaments. Meanwhile SIWs continue to propagate on both the droplet and surface of the bubble.

In the head of SIWs, electron density reaches as high as 2×10^{16} cm^{-3} (figure 3) with a maximum electron-impact ionization rate of 6×10^{24} cm^3 s^{-1} (figure 4). Experimental measurements of electron density of discharges inside the bubbles range from 10^{15} cm^{-3} to 10^{18} cm^{-3}, varying with the gas composition, electrode arrangement and liquid pH values [23, 27, 28, 32]. The speed of the SIW on the surface of the bubble is on the order of 1 mm ns^{-1} (10^8 cm s^{-1}), which agrees with measurements reported by Petrishchev *et al* [60]. At the end of the voltage pulse, due to there being multiple discharges inside the bubble, plasma nearly fills the entire space. This end product differs from discharges in the absence of a droplet where the plasma is mostly confined to the vicinity of the bubble surface [26, 29].

The surface-hugging streamer on the bubble is sustained by the enhanced electric field on the interface between two materials with different permittivities [29, 30, 33, 61]. Here we focus on the processes initiated by the water droplet. The electric field and charge density on the surface of the droplet are shown in figure 5. The ionization sources due to electron impact and photoionization, along with electron temperature and the reduced electric field are shown in the vicinity of the droplet in figure 6. For deionized water with a conductively $\sigma = 10^{-6}$ S cm^{-1} and permittivity $\varepsilon = 80\varepsilon_0$, the dielectric relaxation time $\tau = \sigma/\varepsilon$ is about 7 μs. This is much longer than the ns time scales considered here, and so the surface charging persists. With the gap between the electrodes and droplets now conductive (and sustaining a lower voltage), this positive surface charging reaches a magnitude up to 10^{15} cm^{-3}. The surface charge contributes to enhancing the electric field on the upper part of the droplet until initiation of the second filament at around 1.5 ns.

The launching of the second filament from the upper quadrant of the droplet, illustrated in the sequence in figure 6, results from a series of events related to charging of the
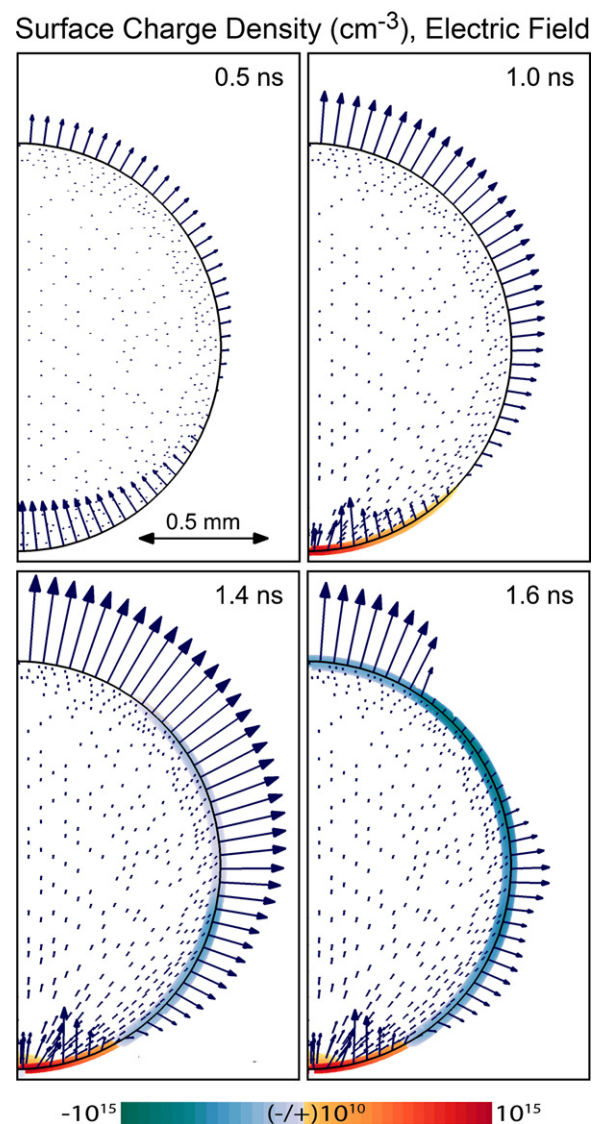

Figure 5. Surface charge density and electric field vectors in the water droplet at 0.5, 1.0, 1.4 and 1.6 ns. The length of the electric field vector is proportional to the local electric field strength.

droplet, polarization of the droplet and photoionization. After the first filament initiated from the electrode reaches the droplet, a SIW is launched along the surface of the droplet. The electron temperature T_e in the head of the SIW is about 4.5 eV—producing electron impact ionization as well as photoionization. The electron impact ionization is local whereas the isotropically emitted VUV photon flux is nonlocal. With the discharge polarity being positive, the intersection of the initial streamer launched from the electrode with the droplet produces positive charge on the bottom of the droplet. As the SIW propagates around the droplet, a surface layer of conductive plasma translates the anode potential to the droplet surface. This results in electric field enhancement in the upper hemisphere of the droplet. Meanwhile there is natural polarization of the droplet that produces electric fields of up to 500 Td at the surface of the droplet above the equator. This value of *E/N* would normally be sufficient to produce an avalanche. The lack of avalanche is due to the lack of seed electrons.
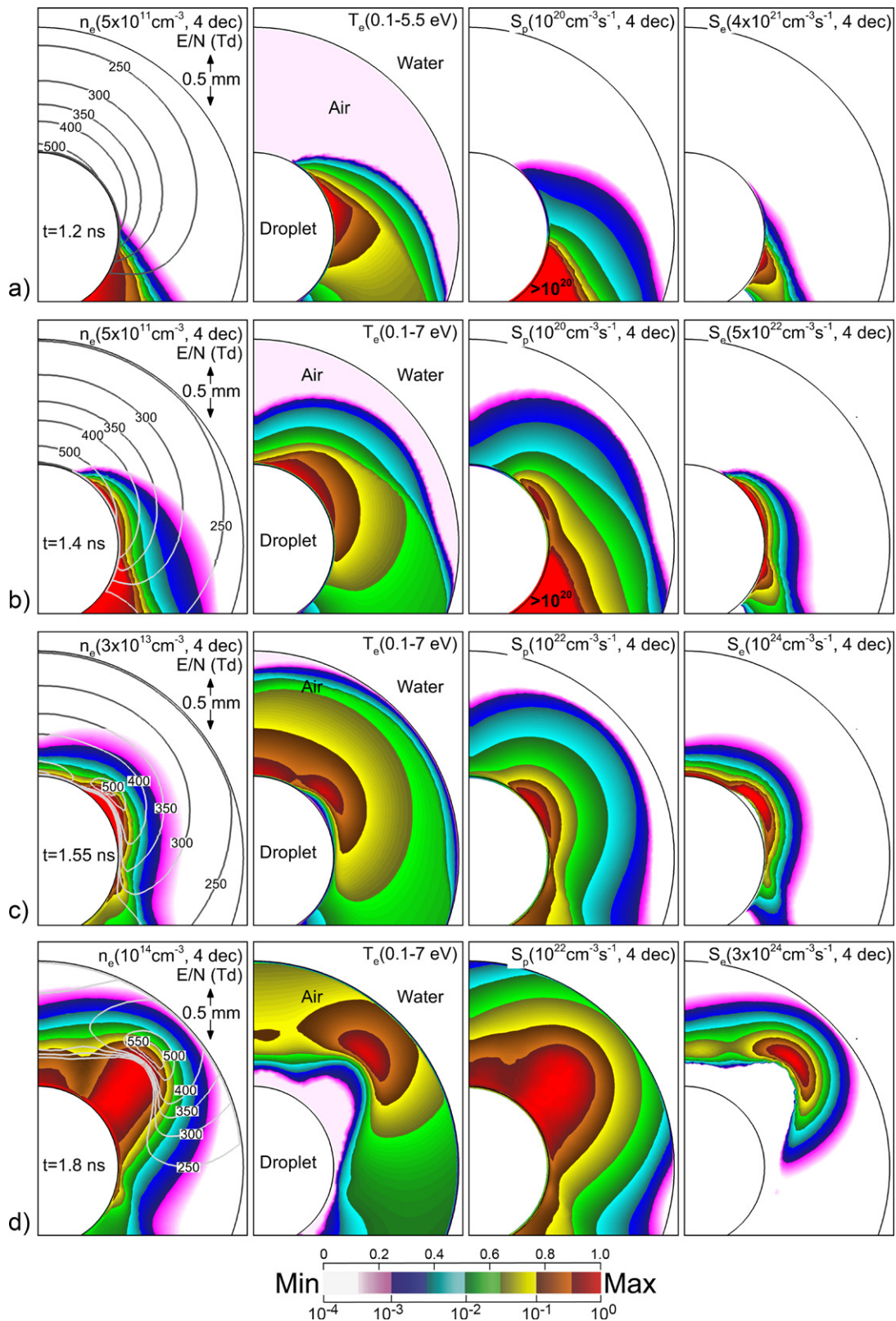
Figure 6. Plasma properties as the secondary streamer is launched at (a) 1.2 ns, (b) 1.4 ns, (c)1.55 ns and (d) 1.8 ns. From left to right at each time are the electron density (n_e, flood) and reduced electric field (E/N, contours), electron temperature (T_e), photoionization rate (S_p), electron-impact ionization rate (S_e). The maximum value for log plots or range of values for linear plots are noted in each frame. The contours for E/N are labeled in units of Td (1 Td = 10^{-17} V cm^2).
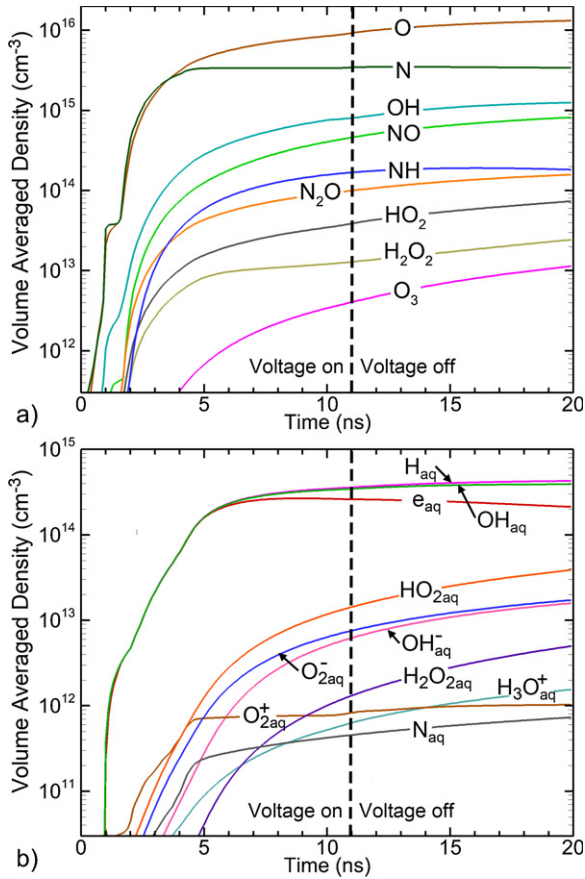
Figure 7. Volume-averaged densities of (a) gas phase neutral species and (b) liquid phase species as a function of time. The times that the voltage is on and off are indicated.

As the SIW reaches the equator of the droplet, the view angle of VUV radiation subtends the region of electric enhancement where E/N exceeds 300 Td, and starts to seed electrons in this region of high electric field. This electric field is sufficiently high to begin to avalanche the humid air, producing the second filament between the droplet and the bubble. At the initial stages of this avalanche (figure 6, 1.4 ns) the charge density is not sufficient to form an IW, a condition that is signaled by the lack of deformation of the electric field. The precursor electrons that start this avalanche are dominantly produced by photoionization. Tests were conducted in which photoionization was excluded from the calculation, and no secondary filament was produced due to the lack of seed electrons.

Once avalanche begins, the plasma density increases to the point that there is sufficient charge density to support an IW (figure 6, 1.55 ns). This stage is indicated by the local maximum in electric field at the leading edge of the IW. The propagation of the positive IW, directed toward the surface of the bubble, is facilitated by photoionization which leads the electron impact ionization source. When the IW separates from the droplet (figure 6, 1.8 ns), a plasma column is left behind having a high conductivity and low E/N.

Once the secondary filament is formed, the voltage drop between the droplet and the bubble surface decreases by virtue
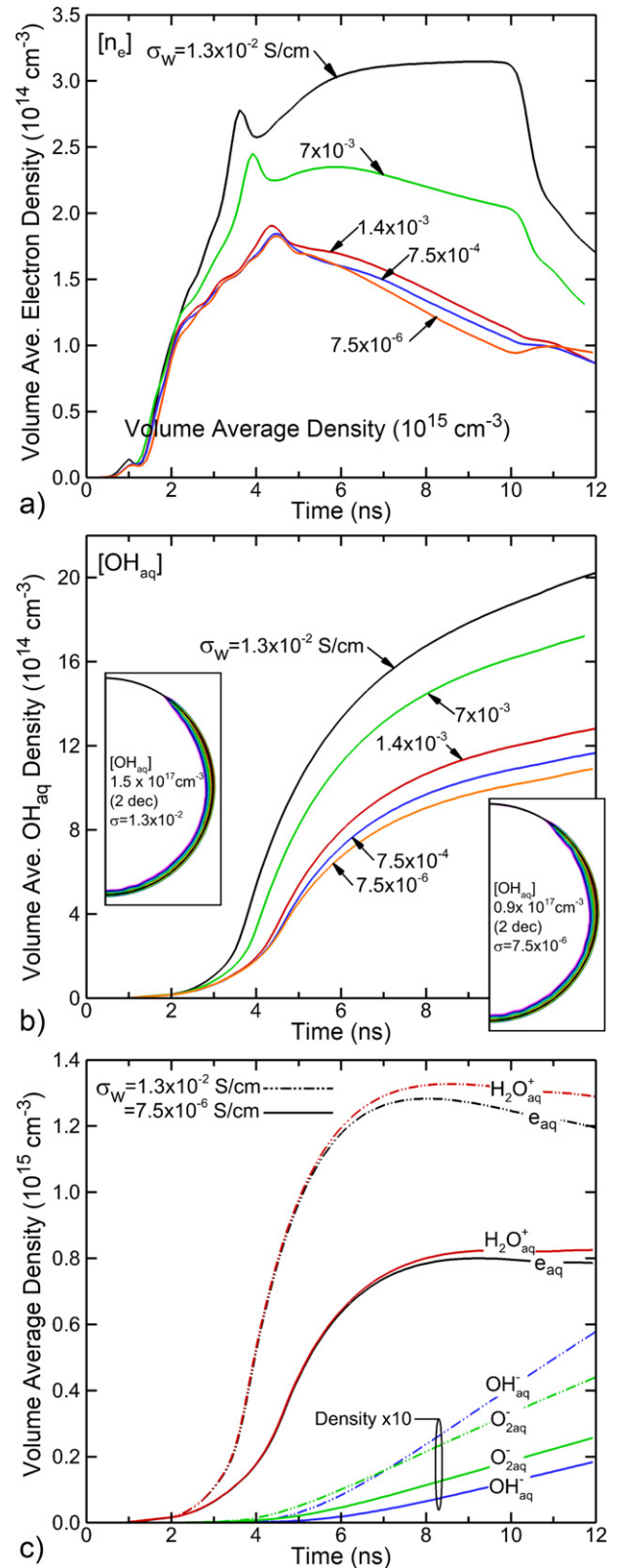

Figure 8. Plasma properties for different values of the conductivity of the water surrounding the bubble, σ_w. (a) Volume-averaged electron density in the air. (b) OH$_{aq}$ in the water droplet. (c) Density of aqueous ions and electrons for $\sigma_w = 1.3 \times 10^{-2}$ S cm^{-1} and 7.5×10^{-6} S cm^{-1}. The other conditions are identical with those in the base case. The embedded images in (b) show the spatial distribution of OH$_{aq}$ density at 10 ns for σ_w being 1.3×10^{-2} S cm^{-1} and 7.5×10^{-6} S cm^{-1}.

of charging of the surface of the bubble. This reduction in voltage across the gap suppresses the formation of additional discharges (see figure 3(d)). Due to the low conductivity of the droplet, discharge current tends to flow along the droplet surface through the plasma produced by the SIW to bridge the first and second filaments, completing the circuit. Electrons produced by the SIW on the droplet and carrying the majority of the current rapidly solvate into the liquid on the time scale of picoseconds. Note that experimental estimates of the penetration depth of electrons before solvation is in the range of 2.5 nm to 12.5 nm [62]. Resolving this dimension in a simulation of the entire reactor is not practical—the mesh resolution of the droplet is much coarser. As such, the rate coefficient for the solvation reaction was chosen so that electrons entering the liquid solvate at the first node of liquid surface. Consequently, there is large accumulation of solvated electrons on the droplet surface, especially near the foot of the second filament (figure 5, 1.6 ns), which contributes to the polarization of the droplet. We believe this is an accurate representation of the physics, as even resolving the mesh nm resolution would produce a layer of solvated electrons that produce a nearly identical potential. At the interface between the positive surface charge due to the initial filament and negative surface charge due to the SIW, a strong electric field parallel to the droplet surface is formed, which then helps sustain the surface streamer [63].

The densities of the dominant reactive species produced by the gas phase plasma are shown in figure 7(a). Electron-impact dissociation of O_2, N_2 and H_2O produce the primary RONS species O, N and OH [64]. Dissociative recombination of O_2^+ and H_2O^+ following discharge propagation producing O and OH contribute to the continuously increasing densities of O and OH during the afterglow pulse-off phase. The initial reactive species will then participate in reactions to form more complex species. For example, N and O can contribute to NO via the Zeldovich mechanism ($N + O_2 \rightarrow NO + O$, $O + N_2 \rightarrow NO + N$) [65], O_3 is generated dominantly via a three-body reaction ($O + O_2 + M \rightarrow O_3 + M$, where M is a third body) and H_2O_2 is formed by self-reactions of OH ($OH + OH + M \rightarrow H_2O_2 + M$). These three-body reactions are relatively slow and so H_2O_2 and O_3 have initially low densities (1×10^{12} to 1×10^{13} cm^{-3}) here where only a single voltage pulse is considered. These relatively stable species accumulate over multiple discharge pulses [46, 66].

In the water droplet, reactive species are primarily formed by the solvation of their gas phase counterparts. The dominant in-water species are shown in figure 7(b). Electron fluxes incident onto the droplet rapidly solvate, and then slowly react with H_2O_{aq} to produce H_{aq} and OH_{aq}^-. The gas-phase positive ions (with the exception of H_3O^+) entering the liquid undergo charge exchange with H_2O_{aq} to form $H_2O_{aq}^+$, which then reacts with H_2O_{aq} to form $H_3O_{aq}^+$ and OH_{aq}. Another important channel for producing OH_{aq} during the plasma pulse is photodissociation of water ($H_2O_{aq} + h\nu \rightarrow OH_{aq} + H_{aq}$). Electronically excited gas phase species incident onto the droplet with sufficiently high energy initiate dissociative excitation transfer with
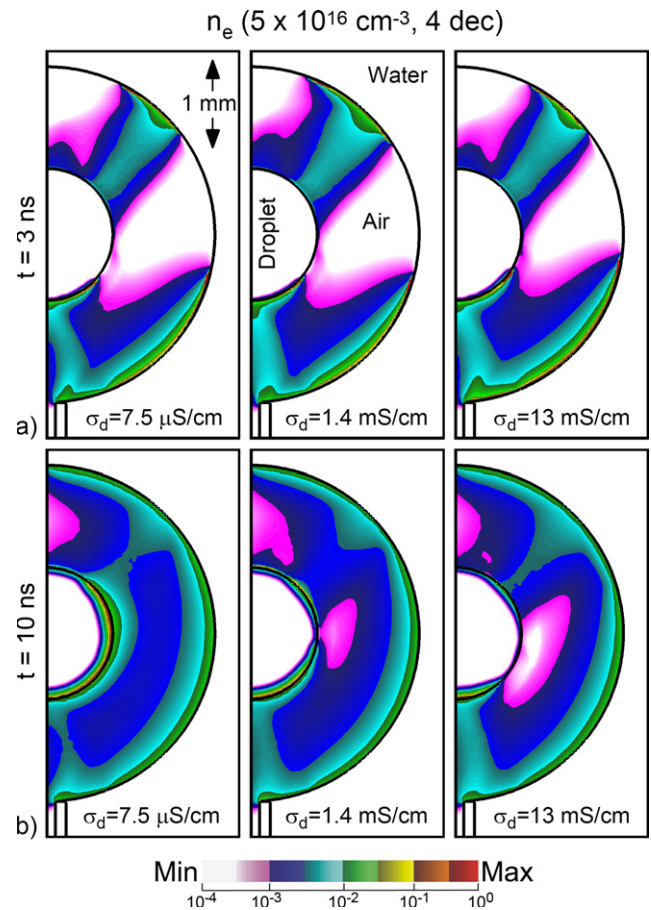

n_e (5 x 10^{16} cm^{-3}, 4 dec)

Figure 9. Densities of the sum of gas and liquid phase electrons (n_e) at (a) 3.0 ns and (b) 10.0 ns for the conductivity of the droplet (σ_d) being 7.5×10^{-6} S cm^{-1}, 1.4×10^{-3} S cm^{-1}, and 1.3×10^{-2} S cm^{-1}. The other conditions are the same as the base case.

H_2O_{aq}, also yielding H_{aq} and OH_{aq}. The fact that H_{aq} and OH_{aq} initially have nearly identical densities suggest that photodissociation by radiation produced by the surface-hugging SIWs and dissociative excitation transfer to water dominate the production of these species. Therefore, the dominant species in the droplet are initially H_{aq} and OH_{aq}. The major negative ions in the droplet are OH_{aq}^- and O_{2aq}^-. The O_{2aq}^- are mainly produced by the fast solvation of gas phase O_{2aq}^-, and electron attachment to O_{2aq}.

Although the intent of the simulations is to address conditions akin to tap water or to align with the experiments, many experiments are performed with distilled water, which has a lower pH of about 5.5. To determine whether the initial pH significantly affects the outcome of the calculation, we performed a simulation of a pulsed discharge for the droplet having an initial pH of 5.5 as in distilled water. We found no significant change in the breakdown characteristics or in gas phase plasma densities. The reason may be that even for a pH of 5.5, the concentration of $H_3O_{aq}^+$ is only about 57 ppm, which is too low to produce a large effect by changing the permittivity or conductivity of the water.
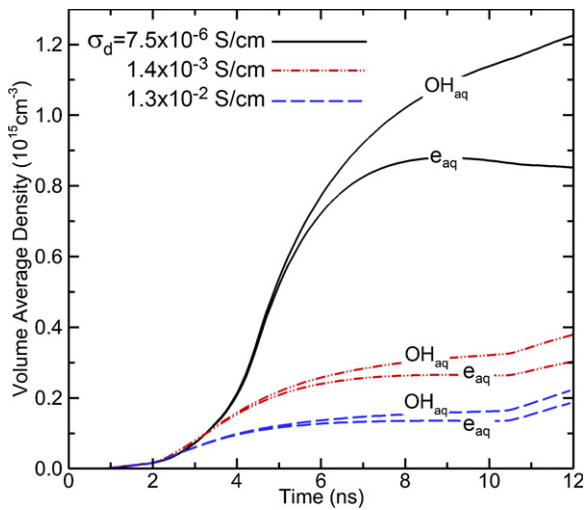
Figure 10. Densities of solvated electrons (e$_{aq}$) and OH$_{aq}$ for values of the conductivity of the droplet, σ_d of 7.5×10^{-6} S cm^{-1}, 1.4×10^{-3} S cm^{-1} and 1.3×10^{-2} S cm^{-1}.

3.2. Conductivity of the surrounding water

Contaminants in water tend to increase the water's conductivity. In this work, we do not computationally treat the surrounding water as a plasma-zone as we do the droplet. However, material properties of the surrounding water are included in the simulation, permittivity and conductivity, σ_w. The range of σ_w we considered is 7.5×10^{-6} S cm^{-1} to 1.3×10^{-2} S cm^{-1} corresponding to the conductivity of deionized water with natural hydrolysis and sea water. Within this range of conductivity, the patterns of the discharge pattern appear to be similar (as those in the base case shown in section 3.1). From the minimum to maximum value of σ_w the electron density in the gas phase plasma increases by a factor of about 1.5, as shown in figure 8. This trend agrees with experiments where higher conductivity of the surrounding water resulted in more intense emission from the plasma and higher discharge current [51]. This increase in electron density is in large part a result of the lower voltage drop across the bulk water with increasing conductivity, leaving a larger voltage drop across the bubble. Experiments conducted by Vanraes *et al* [28] and Hamdan *et al* [31] indicated that the electron density inside bubbles was almost independent of the conductivity of the surrounding water—σ_w being less than 5 mS cm^{-1} in those cases). Measurements of the surface discharges produced in an argon bubble-water film system showed that the electron density increased slightly with water conductivity lower than 28 mS cm^{-1}, with larger increases for σ_w increasing up to 36 mS cm^{-1} [32]. This increase in electron density resulted from a decrease of plasma volume. In our cases, the increase of electron density resulted from the increase in intensity of the surface discharge on the droplet due to the higher across-bubble voltage drop.

With the largest value of σ_w (1.3×10^{-2} S cm^{-1}), the filament between the droplet and the bubble surface becomes more intense, a result of the higher voltage across the bubble that is in part enabled by the lower level of charge accumulation on the bubble surface due to the smaller dielectric
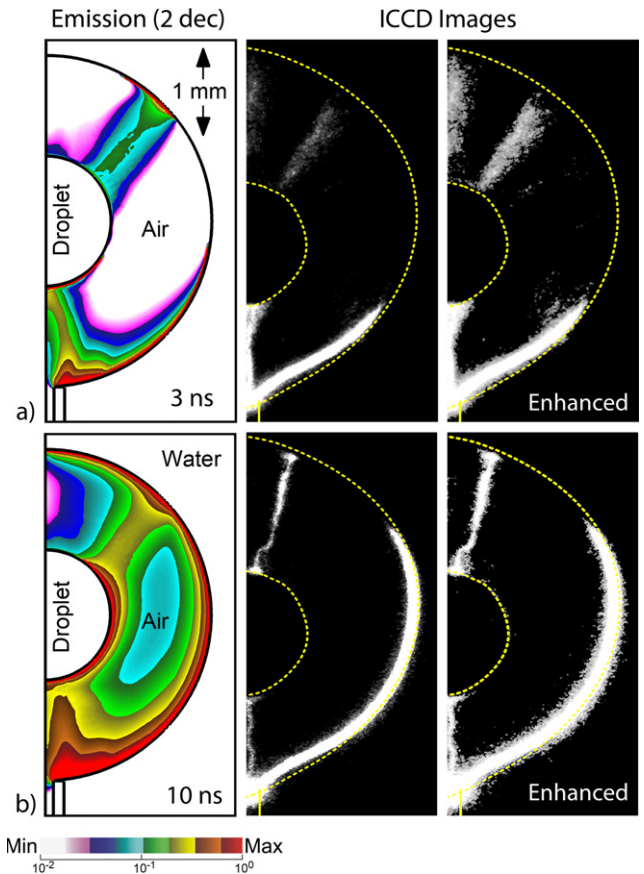

Figure 11. Comparison of simulated optical emission and experimental observations (a) early and (b) late during the voltage pulse. The simulated emission is represented by time integrated emission from excited states of N$_2$, H, OH, O and O$_2$. The corresponding ICCD images had a 5 ns gate. The conductivity of both the water droplet and the surrounding water is 1.3×10^{-2} S cm^{-1}. Two versions of the ICCD images are shown—actual data and artificially enhanced to show more detail.

relaxation time. With the highest conductivity, the dielectric relaxation time of the surrounding water is 0.5 ns, which is short enough to dissipate charge accumulating on the bubble surface during the discharge.

The enhanced surface discharge on the droplet with increasing σ_w generates more OH$_{aq}$ in the droplet. As shown in figure 8(b), there is about a factor of 2 increase in OH$_{aq}$ in the droplet with increasing σ_w. Given the short timescale, the vast majority of this OH$_{aq}$ results from OH production and solvation produced by the surface discharge, photolysis of H$_2$O$_{aq}$ or charge exchange of H$_2$O$^+_{aq}$ to form hydronium. That is, there is little transport of OH from the more distant filaments to the droplet surface. This is also a short enough time that there is nominal production of H$_2$O$_{2aq}$ that depletes the OH$_{aq}$. The densities shown in figure 8(b) are volume averaged densities, obtained by volume integrating all densities of OH$_{aq}$ in the droplet and dividing by the volume of the droplet. During these short times, the OH$_{aq}$ resides nearly entirely at the surface of the droplet, as shown by the insets in figure 8(b), having densities of more than 100 times larger than the average. These higher surface densities in turn facilitate the rapid depletion of OH$_{aq}$ by formation of H$_2$O$_{2aq}$.
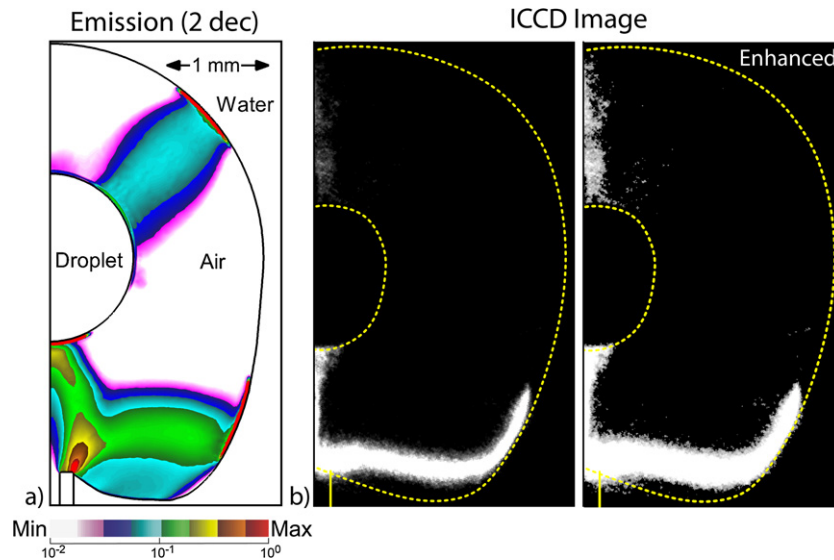
Figure 12. Comparison of simulated optical emission and experimental observations for a deformed bubble. The simulated emissions are represented by time integrated emission from excited states of N_2, H, OH, O and O_2. The corresponding ICCD image had a 5 ns gate. The conductivity of both the water droplet and the surrounding water is 1.3×10^{-2} S cm^{-1}. Two versions of the ICCD image are shown—actual data and artificially enhanced to show more detail.

Aqueous volume averaged ion densities are shown in figure 8(c) as a function of the conductivity of the water surrounding the bubble. As with the gas phase densities, the aqueous ion densities are largest for the large conductivity of water surrounding the bubble. On these short times, $H_2O^+_{aq}$ formed by photoionization and charge exchange has not yet charged exchanged to form hydronium, $H_3O^+_{aq}$, and so the water ion is the dominant positive ion. Negative charge is dominated by solvated electrons, as there is negligible hydrolysis of gas phase produced species (e.g., HNO_x) that might contribute negative ions (e.g., NO^-_{3aq}). As time progresses, solvated electrons begin to undergo charge exchange reactions, resulting in a longer term conversion to O^-_{2aq} and OH^-_{aq}.

Hamdan *et al* observed that increasing the conductivity of the water surrounding an argon bubble led to lower discharge probability and lower charge injection into the water [31]. In Hamdan's experiments, a gas bubble was confined between a sharp pin and a hollow needle, and axial discharges though the volume of the bubble were produced rather than surface-hugging discharges. Under such conditions, power dissipation into the conductive media through the bubble surface tended to reduce the power in the axial channel. In our cases, the surface hugging discharge dominates over the filamentary discharges, and increasing the water conductivity increases electric field inside the bubble to facilitate the discharge [35, 51, 67].

3.3. Conductivity of the water droplet

The conductivity of the droplet was varied from $\sigma_d = 7.5 \times 10^{-6}$ S cm^{-1} to 1.3×10^{-2} S cm^{-1} while keeping other parameters the same as in the base case. The resulting gas phase and liquid phase electron densities are shown in figure 9. Increasing σ_d tends to suppress the surface discharge on the droplet while increasing the intensity of the primary and sec-

ondary filaments, and of the surface discharge on the bubble surface. With a high conductivity of the droplet, discharge current will prefer to flow through the droplet body that has the shortest electrical path (i.e., lowest resistance) to bridge the two filamentary discharges. As a result, power deposition in the surface discharge on the droplet is reduced.

With the lowest σ_d, the dielectric relaxation time is about 1 μs, which is much longer than the duration of the discharge. For these conditions, the droplet acts as a dielectric, supporting surface charging and enabling a SIW to nearly circumnavigate the droplet. For the highest conductivity, the dielectric relaxation time is about 0.5 ns, which enables the surface charge to dissipate into the droplet, which suppresses the propagation of the SIW. At the higher conductivity, the droplet is more equipotential, which enables transfer of the anode potential to the top of the droplet, facilitating the launching of the secondary filament without there being a seeding SIW along the droplet.

The volume averaged aqueous densities of OH_{aq} and e^-_{aq} are shown as a function of time in figure 10 for $\sigma_d = 7.5 \times 10^{-6}$ S cm^{-1} to 1.3×10^{-2} S cm^{-1} (Again, these are volume averaged densities whereas the vast majority of the species reside near the surface with peak densities more than 100 times larger). The trend here is opposite to that of varying the conductivity of the water bounding the bubble. Here, reactive densities increase with decreasing σ_d, a trend that results from the filamentary discharges being suppressed, while the surface discharges are enhanced with decreasing σ_d. At these short times, the transfer of reactive species to the droplet are transport limited. As a result, having more intense SIWs circumnavigating the droplet at low σ_d enables more rapid solvation of electrons and production of OH_{aq} by photolysis, dissociative excitation transfer or solvation.
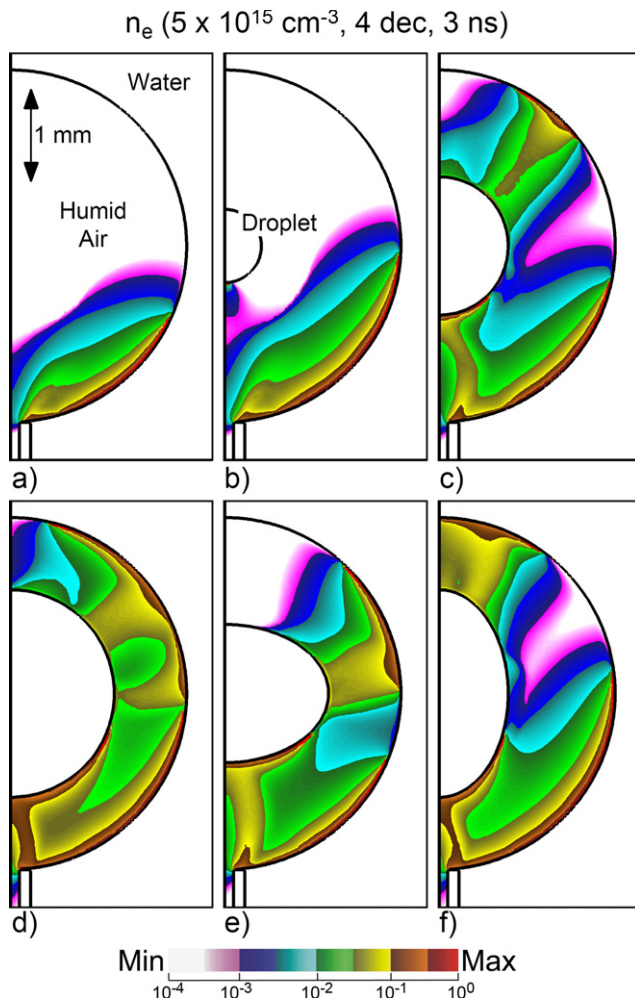
n_e (5 x 10^{15} cm^{-3}, 4 dec, 3 ns)

Figure 13. Electron density (4 decade $\log_{10}$ scale) in the bubble at
3.0 ns for different sizes and shapes of the droplets. The shapes of
the droplets are described by, for example, $0.5x$–$1.0y$, indicating that
the x axis has a length 0.5 that of the base case and the y axis has a
length equal to the base case. (a) no droplet. (b) $0.5x$–$0.5y$,
(c) $1x$–$1y$ (base case), (d) $1.5x$–$1.5y$, (e) $1.5x$–$1.0y$, and (f) $1x$–$1.5y$.

3.4. Comparison to experiments

Qualitative comparisons were made of predicted filament for-
mation by the model and ICCD imaging, as shown in figure 11.
The conductivity of the droplet and water surrounding the bub-
ble is 1.3×10^{-2} S cm^{-1}. The calculated emission is due to
excited-states of N_2, H, OH, O and O_2. (The nitrogen species
dominant the emission intensity.) The ICCD images of visible
light emission are taken by a single exposure with a 5 ns gate
time and a 75 ns delay time. The results agree well between
experiment and modeling. The highest emission intensity is
in the initial filament between the electrode and the droplet,
followed by the advancing SIW along the surface of the bub-
ble. The secondary filament is less intense and appears later.
The experimental trends are reproduced by the model using the
same conductivities as in the experiment, though over shorter
timescales due to the shorter voltage rise-time (0.1 ns) in the
model compared to that in experiments (about 25 ns). For
example, Höft *et al* observed that a steeper rising edge of
voltage pulse led to higher starting velocity of a positive

streamer-like propagation [68]. Zhu *et al* found that a shorter
voltage rise time resulted in stronger ionization and faster
propagation in a nanosecond-pulsed plasma synthetic jet [69].

There are strong interactions between surface streamers and
the shape of the bubble. For example, Sommers *et al* observed
capillary oscillations induced by the successive pulsing of
streamer discharges inside an air bubble immersed in water,
and in turn the streamer closely followed the surface distortion
[37]. Tachibana *et al* found that in an atmosphere of molecu-
lar gases such as N_2 and O_2, surface discharges dominated and
produced wrinkles on the bubble surface, or fragmented a sin-
gle bubble into smaller ones when the applied voltage was high
[25]. Akishev *et al* investigated the destruction mechanism of
large bubbles struck by a positive streamer. They concluded
that the collapse of a bubble was initiated by thermal disrup-
tion of the bubble wall by the streamer [70]. Lai and Foster
investigated the formation of capillary waves on the surface of
a 2D bubble initialed by the surface streamers. Their results
indicated that the perturbation of bubble boundary occurred in
a time scale of millisecond [55].

The sensitivity of streamer propagation to the shape of the
bubble is demonstrated by the model and experimental results
shown in figure 12. (The calculated emission is due to excited-
states of N_2, H, OH, O and O_2. The nitrogen species dominant
the emission intensity.) Here, the experimental bubble had a
bulge adjacent to the electrode, a shape that was reproduced in
the numerical mesh. In experiment and simulation, the initial
streamer nearly simultaneously propagates from the electrode
to the droplet and as a SIW along the bubble. With the greater
curvature of the distortion, the IW toward the bubble is not able
to initially track the surface of the bubble. After propagating a
few mm, the IW attaches to the bubble as a SIW. Much of this
behavior results from details of the electric field enhancement
that occurs at the boundary between the bubble and water, and
is quite sensitive to the curvature of the interface.

The spatial distribution of electron density and optical emis-
sion do not necessarily correspond one-to-one due to the finite
lifetime of both the electrons (which are consumed by attach-
ment, recombination and solvation) and the excited states
(which quench by collisions and relax by optical emission).
For these short time scales, the spatial distribution of electron
density and optical emission are not significantly different.

3.5. Size and shape of the droplet

In the air bubble without a water droplet, the discharge propa-
gates as a surface-hugging streamer as shown in figure 13(a).
This mode of propagation has been discussed by others [26,
29, 35, 36]. With the water droplet in the bubble, the Lapla-
cian electric field is distorted by polarization of the droplet
(figure 1(c)), which in turn affects the discharge evolution.
For example, the Laplacian electric field is not terribly dis-
torted in a bubble with a droplet of half the default diameter.
A discharge in this bubble is still dominantly an SIW along
the surface of the bubble, as shown in figure 13(b). However,
even with this small droplet, the polarization electric field is
large enough to initiate a discharge at the bottom pole of the
droplet. With the default droplet size and a droplet 1.5 times

larger in diameter, the polarization forces dominate, with filamentary discharges produced at the bottom of the droplet and top hemisphere, followed by the SIW along the bubble, shown in figure 13(d).

By changing the shape of the droplet, the polarization electric fields are modified and influence the discharge dynamics. For example, with a droplet that is oval in the horizontal direction, the increased curvature in the horizontal plane is sufficient to produce electric field enhancement. Typically, a circular droplet in a vertical electric field will have a minimum in the electric field at the equator. The horizontally oriented droplet produces electric field enhancement at the equator which enables a filament to be produced at the equator, a phenomenon not observed with spherical droplets. (See figure 13(e).) By elongating the droplet in the vertical direction, the polarization electric fields are minimized on the equator and maximized at the poles. This shifts the location of the secondary filament to being on axis. (See figure 13(f).) The propagation of the SIW along the surface of the droplet is nearly suppressed by the diminished electric field at the equator.

With all shapes of droplets the SIW along the surface of the bubble beginning at the electrode is not terribly affected. This SIW is dominated by the electric field enhancement between the plasma and the water, and the shape of the interface. Since the resulting electric field enhancement does not penetrate far into the bubble, the SIW dynamics are not particularly affected by the shape of the droplet.

4. Concluding remarks

Plasmas produced in gas bubbles immersed in water and plasma activated droplets are two promising ways of water treatment. When producing plasmas in bubbles, aerosols and water droplets are often formed in the bubble. In this paper, results were discussed from computational and experimental investigations of discharges generated in air bubbles with an embedded water droplet. The focus of the investigations was on the formation and propagation of discharges as a function of the conductivities of the droplet and surrounding water and shape of the droplet. Discharge patterns observed from ICCD imaging were qualitatively reproduced by the simulations.

Discharges in bubbles with droplets occurs in three stages. Initially, the (Laplacian) electric field is distorted by the droplet, leading to an enhanced electric field in the gap between the powered electrode and the droplet. A plasma filament or streamer is triggered in this gap in addition to a surface hugging streamer along both the droplet and on the bubble surface. The latter is frequently observed at the air-water interface [29, 51]. The plasma filament serves as a conductive channel that transfers the high voltage from the electrode to the lower pole of the droplet. With charging and polarization of the water droplet, an intense electric field is formed on the upper hemisphere of the droplet. As the surface-hugging streamer progresses along the droplet, photoionization occurs ahead of the streamer. This photoionization seeds electrons in the region of high electric field. Consequently, a second filament is launched from the upper quadrant of the droplet to the bubble surface.

With the formation of the two filaments with high conductivity and low E/N, steep electrical potential drop occurs on the droplet surface, and an enhanced SIW is formed on the droplet surface to bridge the two filaments.

The SIW on the bubble surface is quite sensitive to the curvature of the air-water interface due to geometry-induced local enhancement of electric field. For similar reasons, altering the size or shape of the droplet can alter the locations where discharges appear or are launched from the droplet. These processes also affect where solvated electrons are produced and their densities, which will subsequently impact the plasma chemistry within the droplet.

Activation of the droplet by reactive aqueous species such as OH_{aq} is dominated by the SIW on the droplet surface. Increasing the conductivity of the droplet tends to reduce the electric field in the head of SIW and suppress its propagation, which therefore leads to lower densities of aqueous reactive species. Increasing conductivity of the water surrounding the bubble does not affect discharge patterns, but slightly increases the discharge intensity. Plasma activation of water using discharges in bubbles generally benefits from having immersed droplets. Experimentally it is difficult to access plasma dose delivered to a given droplet of water or within a single bubble. The 2D bubble apparatus enables one to isolate and study dose delivery to a single droplet or bubble under a range of experimental conditions, and also enables direct comparison to computations.

ORCID iDs

Janis Lai ⓘ https://orcid.org/0000-0002-9806-0591
Juliusz Kruszelnicki ⓘ https://orcid.org/0000-0003-4596-1780
John E Foster ⓘ https://orcid.org/0000-0001-8369-1828
Dong Dai ⓘ https://orcid.org/0000-0002-2682-5778
Mark J Kushner ⓘ https://orcid.org/0000-0001-7437-8573

References

[1] Bruggeman P J *et al* 2016 *Plasma Sources Sci. Technol.* **25** 053002
[2] Lu X, Keidar M, Laroussi M, Choi E, Szili E J and Ostrikov K 2019 *Mater. Sci. Eng. R Rep.* **138** 36

[3] Yang A, Liu D, Wang X, Li J, Chen C, Rong M and Kong M G 2016 *J. Phys. D: Appl. Phys.* **49** 415201

[4] Zhou R, Li J, Zhou R, Zhang X and Yang S 2019 *Innovative Food Sci. Emerging Technol.* **53** 36

[5] Foster J E 2017 *Phys. Plasmas* **24** 055501

[6] Shao T, Wang R, Zhang C and Yan P 2018 *High Voltage* **3** 14

[7] Vasile Nastuta A, Pohoata V and Topala I 2013 *J. Appl. Phys.* **113** 183302

[8] Thiyagarajan M, Sarani A and Gonzales X 2013 *J. Appl. Phys.* **113** 093302

[9] Liu D, He T, Liu Z, Wang S, Liu Z, Rong M and Kong M G 2018 *Plasma Processes Polym.* **15** 1800057

[10] Ning W, Dai D, Zhang Y, Han Y and Li L 2018 *J. Phys. D: Appl. Phys.* **51** 125204

[11] Norberg S A, Tian W, Johnsen E and Kushner M J 2014 *J. Phys. D: Appl. Phys.* **47** 475203

[12] Huang B, Zhang C, Adamovich I, Akishev Y and Shao T 2020 *Plasma Sources Sci. Technol.* **29** 044001

[13] Kovačević V V, Sretenović G B, Slikboer E, Olivier G, Sobota A and Kuraica M M 2018 *J. Phys. D: Appl. Phys.* **51** 065202

[14] Wu K, Ren C, Jia B, Lin X, Zhao N, Jia P and Li X 2019 *Plasma Processes Polym.* **16** e1900073

[15] Li X, Chen J, Lin X, Wu J, Wu K and Jia P 2020 *Plasma Sources Sci. Technol.* **29** 065015

[16] Liu F, Zhang B, Fang Z, Wan M, Wan H and Ostrikov K K 2018 *Plasma Processes Polym.* **15** e1700114

[17] Kovach Y E, Garcia M C and Foster J E 2019 *IEEE Trans. Plasma Sci.* **47** 3214

[18] Rumbach P, Lindsay A E and Go D B 2019 *Plasma Sources Sci. Technol.* **28** 105014

[19] Girard F *et al* 2018 *Phys. Chem. Chem. Phys.* **20** 9198

[20] Liu D X, Liu Z C, Chen C, Yang A J, Li D, Rong M Z, Chen H L and Kong M G 2016 *Sci. Rep.* **6** 23737

[21] An W, Baumung K and Bluhm H 2007 *J. Appl. Phys.* **101** 053302

[22] Panov V A, Vasilyak L M, Vetchinin S P, Pecherkin V Y and Son E E 2019 *Plasma Sources Sci. Technol.* **28** 085019

[23] Hayashi Y, Takada N, Kanda H and Goto M 2015 *Plasma Sources Sci. Technol.* **24** 055023

[24] Wen J, Li Y, Li L, Ni Z, Li Y and Zhang G 2020 *J. Phys. D: Appl. Phys.* **53** 425208

[25] Tachibana K, Takekata Y, Mizumoto Y, Motomura H and Jinno M 2011 *Plasma Sources Sci. Technol.* **20** 034005

[26] Tian W, Tachibana K and Kushner M J 2014 *J. Phys. D: Appl. Phys.* **47** 055202

[27] Hamdan A and Cha M S 2016 *J. Phys. D: Appl. Phys.* **49** 245203

[28] Vanraes P, Nikiforov A and Leys C 2012 *J. Phys. D: Appl. Phys.* **45** 245206

[29] Babaeva N Y and Kushner M J 2009 *J. Phys. D: Appl. Phys.* **42** 132003

[30] Levko D, Sharma A and Raja L L 2017 *J. Phys. D: Appl. Phys.* **50** 085202

[31] Hamdan A, Čerņevičs K and Cha M S 2017 *J. Phys. D: Appl. Phys.* **50** 185207

[32] Wang H, Wandell R J, Tachibana K, Voráč J and Locke B R 2019 *J. Phys. D: Appl. Phys.* **52** 075201

[33] Babaeva N Y, Tereshonok D V and Naidis G V 2015 *J. Phys. D: Appl. Phys.* **48** 355201

[34] Maehara T, Honda S, Inokuchi C, Kuramoto M, Mukasa S, Toyota H, Nomura S and Kawashima A 2011 *Plasma Sources Sci. Technol.* **20** 034016

[35] Bruggeman P, Leys C and Vierendeels J 2007 *J. Phys. D: Appl. Phys.* **40** 1937

[36] Babaeva N Y, Naidis G V, Tereshonok D V and Smirnov B M 2017 *J. Phys. D: Appl. Phys.* **50** 364001

[37] Sommers B S, Foster J E, Babaeva N Y and Kushner M J 2011 *J. Phys. D: Appl. Phys.* **44** 082001

[38] Tu Y, Xia H, Yang Y and Lu X 2016 *Phys. Plasmas* **23** 013507

[39] Xiong R, Nikiforov A Y, Vanraes P and Leys C 2012 *Phys. Plasmas* **19** 023501

[40] Hamdan A and Cha M S 2015 *J. Phys. D: Appl. Phys.* **48** 405206

[41] Levko D, Sharma A and Raja L L 2016 *J. Phys. D: Appl. Phys.* **49** 025206

[42] Sommers B S and Foster J E 2014 *Plasma Sources Sci. Technol.* **23** 1

[43] Patel K, Mannsberger A, Suarez A, Patel H, Kovalenko M, Fridman A A, Miller V and Fridman G 2016 *Journal of Plasma Medicine* **6** 447

[44] Kovalova Z, Leroy M, Kirkpatrick M J, Odic E and Machala Z 2016 *Bioelectrochemistry* **112** 91

[45] Wandell R J and Locke B R 2014 *Ind. Eng. Chem. Res.* **53** 609

[46] Kruszelnicki J, Lietz A M and Kushner M J 2019 *J. Phys. D: Appl. Phys.* **52** 355207

[47] Tian W and Kushner M J 2014 *J. Phys. D: Appl. Phys.* **47** 165201

[48] Lietz A M and Kushner M J 2016 *J. Phys. D: Appl. Phys.* **49** 425204

[49] Locke B R and Shih K-Y 2011 *Plasma Sources Sci. Technol.* **20** 034006

[50] Xiong Z and Kushner M J 2014 *Plasma Sources Sci. Technol.* **23** 065041

[51] Lai J and Foster J E 2020 *J. Phys. D: Appl. Phys.* **53** 025206

[52] Kuchma A E, Shchekin A K and Martyukova D S 2016 *J. Aerosol Sci.* **102** 72

[53] Zhang C, Huang B, Luo Z, Che X, Yan P and Shao T 2019 *Plasma Sources Sci. Technol.* **28** 064001

[54] Yang Z, Xu P, Wei W, Gao G, Zhou N and Wu G 2020 *IEEE Trans. Plasma Sci.* **48** 2822

[55] Lai J and Foster J E 2019 *Plasma Sources Sci. Technol.* **28** 125003

[56] Darny T, Pouvesle J-M, Puech V, Douat C, Dozias S and Robert E 2017 *Plasma Sources Sci. Technol.* **26** 045008

[57] Babaeva N Y, Naidis G V, Panov V A, Wang R, Zhang S, Zhang C and Shao T 2019 *Plasma Sources Sci. Technol.* **28** 095006

[58] Norberg S A, Johnsen E and Kushner M J 2015 *J. Appl. Phys.* **118** 013301

[59] Babaeva N Y, Naidis G V and Kushner M J 2018 *Plasma Sources Sci. Technol.* **27** 015016

[60] Petrishchev V, Leonov S and Adamovich I V 2014 *Plasma Sources Sci. Technol.* **23** 065002

[61] Bruggeman P, Degroote J, Vierendeels J and Leys C 2008 *Plasma Sources Sci. Technol.* **17** 025008

[62] Rumbach P, Bartels D M, Sankaran R M and Go D B 2015 *Nat. Commun.* **6** 7248

[63] Ning W, Dai D and Li L 2018 *Plasma Sources Sci. Technol.* **27** 08LT01

[64] Sakiyama Y, Graves D B, Chang H-W, Shimizu T and Morfill G E 2012 *J. Phys. D: Appl. Phys.* **45** 425201

[65] Machala Z, Tarabová B, Sersenová D, Janda M and Hensel K 2019 *J. Phys. D: Appl. Phys.* **52** 034002

[66] Tian W and Kushner M J 2015 *J. Phys. D: Appl. Phys.* **48** 494002

[67] Mededovic Thagard S, Prieto G, Takashima K and Mizuno A 2012 *IEEE Trans. Plasma Sci.* **40** 2106

[68] Höft H, Becker M M, Loffhagen D and Kettlitz M 2016 *Plasma Sources Sci. Technol.* **25** 064002

[69] Zhu Y, Wu Y, Jia M, Liang H, Li J and Li Y 2015 *Plasma Sources Sci. Technol.* **24** 015007

[70] Akishev Y, Arefi-Khonsari F, Demir A, Grushin M, Karalnik V, Petryakov A and Trushkin N 2015 *Plasma Sources Sci. Technol.* **24** 065021